J Mater Sci: Mater Electron (2023) 34:1146

Optimization of graphene dose for improved electrochemical performance of silicon–graphene negative electrodes in lithium batteries

Moustafa M. S. Sanad[1,*] and Atef Y. Shenouda[1]

[1] *Batteries Technology Department, Central Metallurgical Research and Development Institute (CMRDI), P.O. Box 87, Helwan, Cairo 11421, Egypt*

Received: 27 February 2023
Accepted: 30 April 2023
Published online: 15 May 2023

ABSTRACT

Different percentages of nanoparticles graphene (G) were mixed with nano-micron sized silicon (Si) particles as follows: 10, 20, 30 and 40 wt% graphene to silicon ratios. The crystal structure of pure Si powder pattern has cubic phase SEM, TEM/SAED and XPS equipments were implemented to study the surface properties of the prepared G@Si composites. Cyclic voltammetry (CV) measurement for the G@Si cell revealed two broad cathodic peaks, related to the deposition of Li_2O thin layer on Si particles and the lithiation process of Si to form lithium silicide. Meanwhile, the oxidation of Li_xSi into Si and Li ionis confirmed by the anodic strong peak at 0.56 V. Electrochemical impedance spectroscopy (EIS) measurements revealed high interfacial resistance ~ 1825 Ω for pure Si anode in comparison with that of G@Si composite anode. It is concluded that graphene acts as a conductive shielding pathway to inhibit the large volume change and minimize the capacity fading during successive galvanostatic cycling of G@Si composite anode materials versus Li/Li^+. Accordingly, the specific discharge capacity of 30%G@Si cell delivered about 1240 and 900 $mAhg^{-1}$ for 1st and 100th charge–discharge cycles, respectively.

1 Introduction

In the past two decades, Li-ion batteries (LIBs) have transformed portable electronic gadgets, and they provided suitable power for electric vehicles [1, 2]. Despite their enormous potential, current LIB technology (e.g., graphite@$LiCoO_2$ batteries) has not been capable to satisfy the demands for vehicle electrification, which call for batteries with simultaneous high power/energy densities, and extended cycle lives [3, 4]. Therefore, there is a pressing need for a variety of anode materials with large energy density, power density, and extended cycle life [5, 6]. Silicon is a promising anode for LIBs owing to its high theoretical capacity and low voltage profile, which is roughly ten times greater than that of carbonaceous materials like graphite, pyrolytic carbon, and mesophase pitch (around 372 $mAh.g^{-1}$) for the $Li_{15}Si_4$ phase at ambient

Address correspondence to E-mail: mustafa_sanad2002@yahoo.com

temperature [7]. Furthermore, as silicon is the second most abundant element in the earth's crust, its mass manufacturing at competitive prices is quite plausible. The excessive volume change (about 300%) during the lithiation and de-lithiation processes, the lack of intrinsic electrical conductivity, and the instability of the solid electrolyte interface (SEI) are now obstacles to the practical use of silicon anodes in LIBs [8, 9]. Particle pulverization, electricity loss from the active material or the current collector, and the peeling of the current collector can happen as a result of the significant volume change. Repeated volume expansion and contraction also cause the SEI layer around the particles to fracture and reform, which causes an ongoing loss of electrolyte, a noticeable decay in capacity and an impedance increase [10–12]. The aforementioned problems have been the focus of much attention. Designing and fabrication of different composites of nanomaterials was known as an effective way to enhance the electronic and catalytic properties [11–16]. The strategies that have been studied include the design of Si materials using nanostructures [17–21], porous structures [22–24], or nanocomposites [25–27]. Additionally, Si thin film designed by electron beam evaporation was implemented as an anode in lithium batteries. It was found that the addition of fluoroethylene carbonate (3 wt%) to 1.3 M $LiPF_6$ offered a smoother and more stable solid electrolyte interface (SEI) layer, resulting in better capacity retention and coulombic efficiency in lithium cells [28]. Polyacrylic acid and natural polysaccharides were introduced as new binders with comparable behavior to carboxymethylcellulose (CMC) and poly(vinylidene fluoride) (PVDF) binders in Si-based Li batteries [29, 30]. Another study declared that the coating of Si nanowires with a thin film of amorphous SiO_2 (thickness $\sim$ 7 nm) via thermal oxidation leads to a large initial storage capacity $\sim$ 2279 $mAh.g^{-1}$ with 83% retention in the capacity after 50 cycles at 0.2 °C versus lithium [31]. It is also important to note that previous trials and achievements to enhance the electrochemical performance of Si anode have quickly increased in the recent ten years [32–34]. The design strategies of Si anode material included different morphologies, (i) nanoparticles, core-shells and yolk-shells, (ii) porous silicon structures, (iii) nanowires, nanofibers, and nanotubes (iv) silicon composites, …etc.[35]. The purpose of the study is to optimize the amount of graphene nanoparticles that will provide the maximum protection for silicon from too much expansion in the structure and hence achieving the best cyclability and electrical conductivity for the commercial silicon in LIBs. Therefore, the present work introduces a simple and applicable hybridization method for the preparation of graphene-shielded silicon particles using a wet grinding technique. The physicochemical characterization of the obtained composites was performed to distinguish the differences between pure Si and its composite. The electrochemical storage behavior of the developed anode composite was analyzed and optimized using various advanced techniques e.g., galvanostatic cycling (GC), CV, and EIS.

2 Experimental

2.1 Sample preparation and characterization

Pure Si powder (BDH) was ground using a planetary ball mill (400 rpm/3 h) and sieved to about − 10 μm. The obtained fine Si powder was hybridized with different weight percentages of graphene (G) nanoplatelets (Sigma Aldrich) as follows: 10, 20, 30 and 40 wt.%. The hybridization technique was performed via wet grinding technique of 3 g for each sample mixture up to 300 rpm/1 h in 100 ml acetone as a solvent medium. The mixed suspension was left in an oven at 80 °C overnight to ensure complete dryness.

The crystallographic features of each sample were detected and identified by X-ray diffraction (XRD) spectrum, which operated at 40 kV and 30 mA. The angle scan rate was about 2°/min. The measurements of X-ray Photo-electron Spectroscopy (XPS) using PHI 5600 instruments were performed. The microstructure of pure Si and 30wt% G@Si samples were inspected by Field Emission Electron Microscope (FESEM), QUANTAFEG 250 and Transmission Electron Microscope (TEM) JOEL JEM2010-200 kV.

2.2 Electrochemical cell assembly and measurements

Firstly, the composition of the electrodes was manufactured by wet mixing the active anode material, and acetylene C-black along with polyvinylidene difluoride (PVDF) in the conducting solvent N-methyl-2-pyrrolidine (NMP) according to the weight ratio (80:10:10). The mixed slurry was semi-

automatically plated on copper foil using TMAX film coater. The coated electrodes were dried at 110 °C under vacuum for 24 h. Cell assembly was done in an Ar-filled glove box. 1 M solution of $LiPF_6$ dissolved in propylene carbonate and ethylene carbonate was injected as battery electrolyte. Electrochemical measurements were conducted for coin cell models CR2032 using lithium metal as a counter and reference electrode. Cycling voltammetry (CV) of the cells was achieved in the potential windows 0.01 and 3.0 V with a scan rate 0.1 mVs^{-1} through Biologic Battery tester Model 205. Furthermore, impedance measurements were applied in the frequency range 2×10^4 and 10^{-3} Hz and amplitude of 10 mV.

Mott-Schottky measurements were estimated for the samples in three electrode cell configuration at frequency 500 Hz. The electrochemical cell consists of active material@In-SnO-glass (working electrode), Pt-wire (counter electrode), saturated Ag–AgCl (reference electrode), and 0.1 M Na_2SO_4 (supporting electrolyte). UV–Vis-NIR spectrophotometer (JASCO V-, Japan) was employed to count the light absorption and diffuse reflectance spectra.

3 Results and discussion

3.1 Structure characterization

XRD diffraction patterns of pure Si and 30wt%G@Si samples are given in Fig. 1. Five distinct peaks are observed at (28.476°, 47.333°, 56.161°, 69.125°, and 76.373°), indicating a single cubic phase of Si metal (PDF card no. 27-1402) [34]. The XRD pattern of 30%G@Si shows the same crystal structure and only a very weak and broad peak could be observed at 26.59 ° that confirms the presence of graphene. The average crystallite size of pure Si and 30%G@Si samples are equal to 42.5 and 31.5 nm, respectively. It is also found that the inclusion of graphene nanoplates in the bulk Si induces a small expansion in the cell volume of Si crystal from 160.3 $Å^3$ to 160.8 $Å^3$ after Graphene addition.

3.2 Microstructure characterization

FESEM images of pure Si and 30wt%G@Si are shown in Fig. 2a–d. As inspected in Fig. 1a and b, the shape of Si crystals appeared as rectangular- or prism-like morphology with particle size range 0.8–2.0 µm. FESEM image (Fig. 2c) of the prepared 30wt%G@Si composite at magnification 5000X reveals the good interference of both graphene and silicon materials in which the graphene nanoplates are embedded between the larger grains of silicon. It can be noticed also that the average particle size of 30wt%G@Si is smaller than pure Si sample (Fig. 2d), showing a good agreement with the XRD results.

Figure 3a, b reveals the TEM images of pure Si particles and 30wt%G@Si composite, respectively. Most of Si crystals have undefined geometry with a wide particle size range 60–150 nm. On the other hand, TEM image of the composite sample displays a narrower particle size range 50–100 nm for the Si crystals. Meanwhile, the dispersed graphene nanosheets in the composite sample do not exceed 10 nm and cover the outer surface of large Si crystals. SAED technique can be used to distinguish the pure Si and its composite sample. Figure 3c depicts the typical SAED of Si crystals revealing the three parallel lines of bright dots, characteristic to the atomic planes (111), (220), and (400) of the cubic structure [36]. In addition, the two diffraction rings observed in the SAED pattern of the G@Si composite (Fig. 3d) confirm the existence of graphene nanosheets as well as the bright dots of Si nanocrystals [37].

3.3 XPS surface analysis

The XPS survey analysis was performed to recognize the atomic levels and oxidation states in the 30%G@Si composite as given in Fig. 4a. Three main peaks can be identified in the overall XPS survey, adjusted at the binding energies of O1s, C1s, and Si2p elements. Figure 4b depicts the XPS of Si2p that can be fitted into two main peaks at 103.4 eV ($Si2p_{3/2}$) and 104.3 eV($Si2p_{1/2}$), characteristic for Si–O–C and Si–O bonds, respectively [38, 39]. The high-resolution XPS scan of C1s (Fig. 4c) can be deconvoluted into 6 peaks corresponding to C=C (sp^2), C–C (sp^3), C–O, C=O, HO–C=O, and π–π* at 284, 284.7, 285.3, 286.2, 287.2, and 289.7 eV, respectively [40]. The presence of π–π* (HOMO–LUMO) transition in XPS spectra of C 1 s gives a strong indication for the enhanced conductivity of the composite sample provided by the availability of π-conjugate delocalized electrons in the sp^2 carbon atoms of graphene nanosheets [41]. Moreover, the detection of minor peaks for carbonyl and carboxyl groups could be explained by the cleavage of some C=C bonds into C–O sp^3 or C=O sp^2

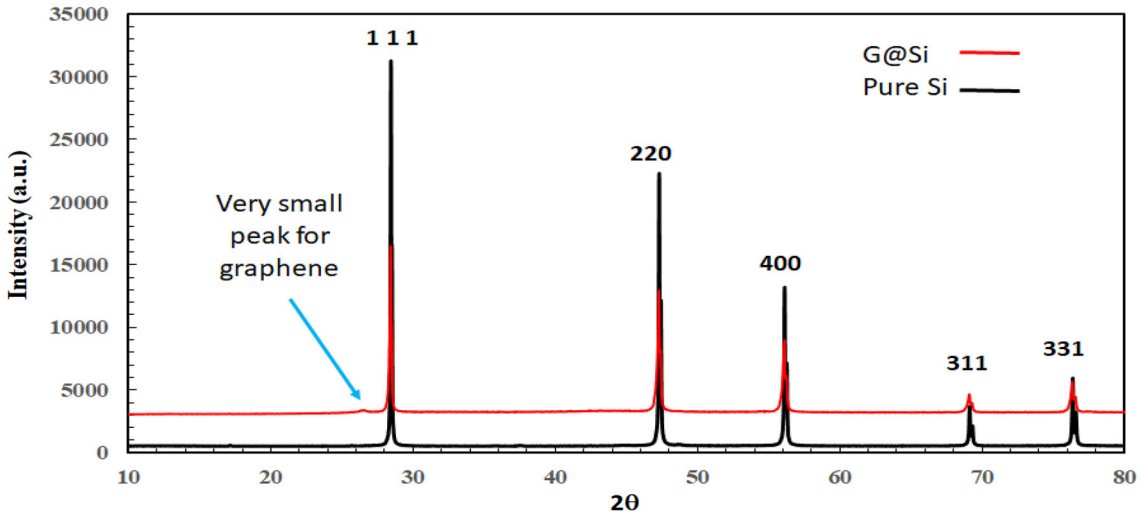

Fig. 1 XRD of pure Si metal and 30%G@Si composite between 10 and 80° at angle scan rate ~ 2°.min.$^{-1}$

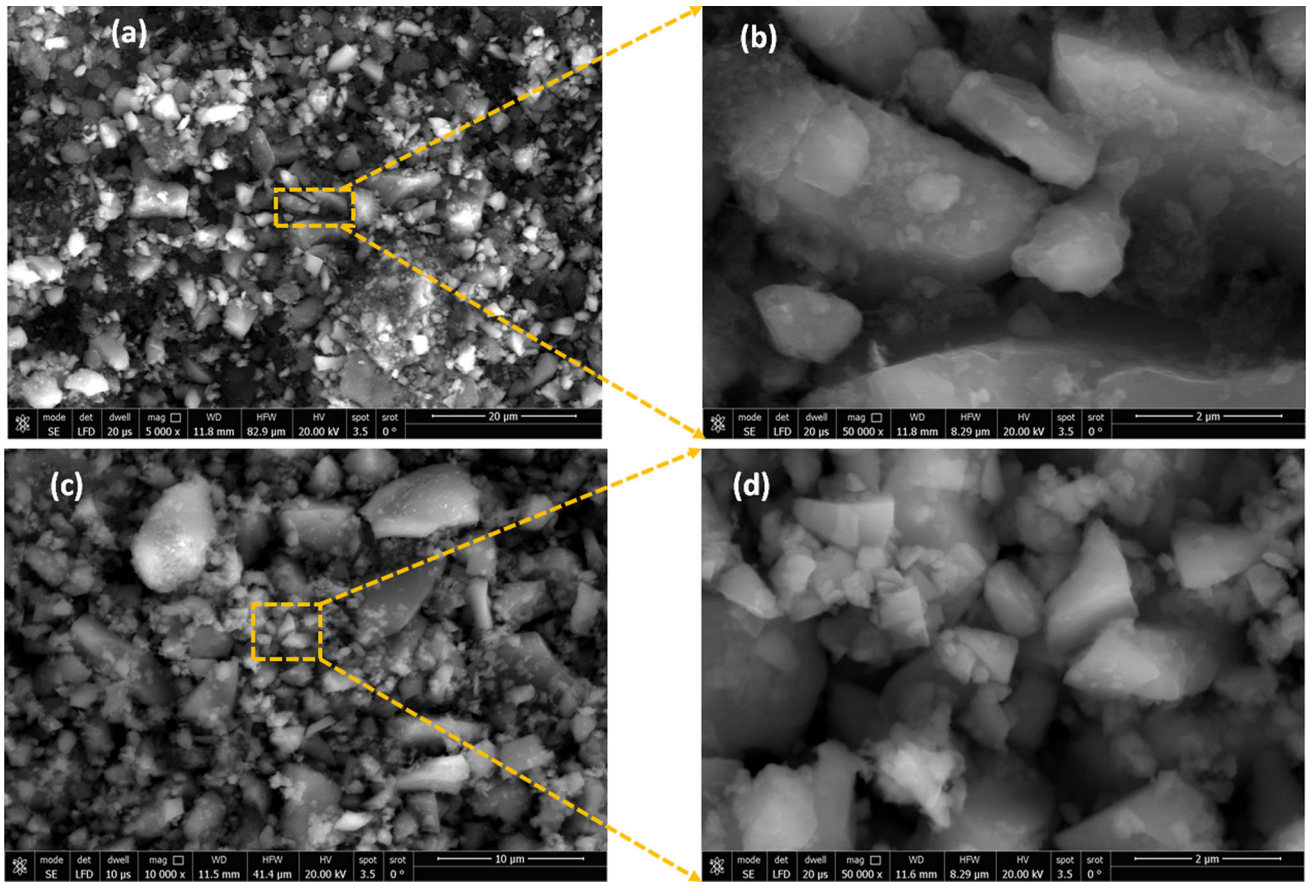

Fig. 2 FESEM images of pure Si at two different magnifications: **a** 5000× & **b** 50000× and 30%G@Si composite at **c** 5000× & **d** 50000×

due to the partial oxidation of graphene sheets into graphene oxide.

The detection of O1s XPS spectra means that some of Si could be oxidized into SiO_2 during the grinding step with graphene and simultaneously, graphene

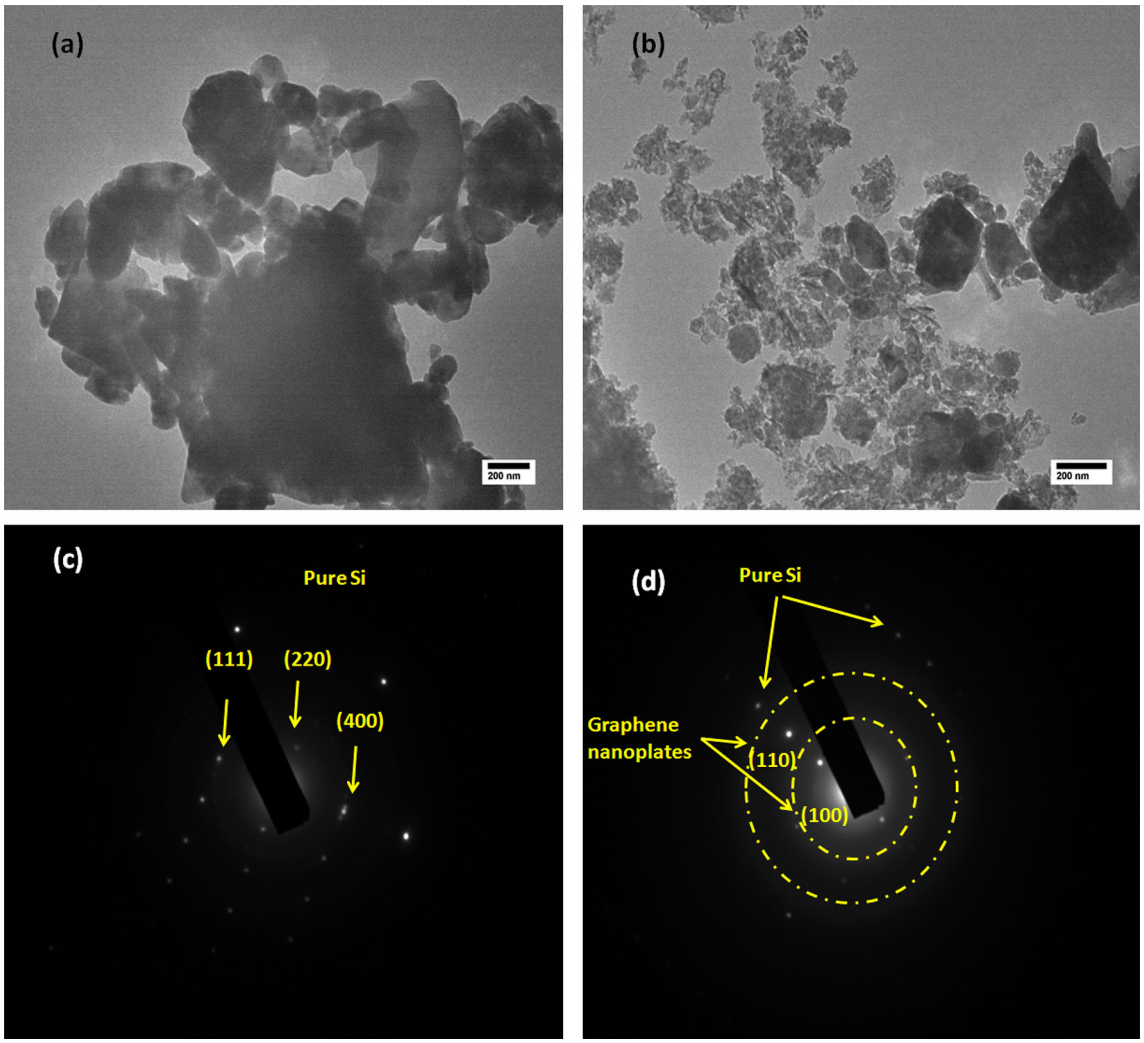

Fig. 3 **a**, **b** TEM images and **c**, **d** SAED patterns of pure Si particles and 30%G@Si composite, respectively

partially transformed into graphene oxide. The deconvolution of O1s spectra into three main peaks at 531.9, 533.2, and 534 eV is related to the Si–O, O–H/oxygen deficiency, and adsorbed H_2O, respectively [42].

3.4 Electrochemical characterization and optimization

Figure 5a–d display the CV measurements for the assembled cells composed of lithium versus G@Si composite with different graphene ratios (10, 20, 30, and 40 wt%) in the potential range 0–3 V upon scanning rate 0.1 $mV.s^{-1}$. CV diagram for 10%G@Si cell produces three weak and broad peaks in the cathodic direction at 0.02 V, 0.19 V and 0.85 V. The first and second cathodic peaks at 0.02 V and 0.19 V are attributed to the lithiation step of Si to form lithium silicide as explained by Eq. 1 [43]:

$$Si + x\ Li^+ + xe^- \rightarrow Li_xSi \quad \text{where, } x = 3.75 \qquad (1)$$

The broad cathodic peak at 0.85 V indicates the formation of SEI layer on the electrode surface [44].

The strong anodic oxidation peak can be observed around 0.56 V due to the oxidation of Li_xSi into Si and Li^+ ion [45] as shown in Fig. 5a. Therefore, Li-ion is de-intercalated from the Li_xSi alloy as explained by Eq. 2:

$$Li_xSi \rightarrow Si + x\ Li^+ + xe^- \qquad (2)$$

Similar anodic peaks are recorded with cells of 30% G@Si as shown in Fig. 5c. However, the cathodic peaks at the higher potential might be disappeared, which could be assigned to the loss in the irreversible

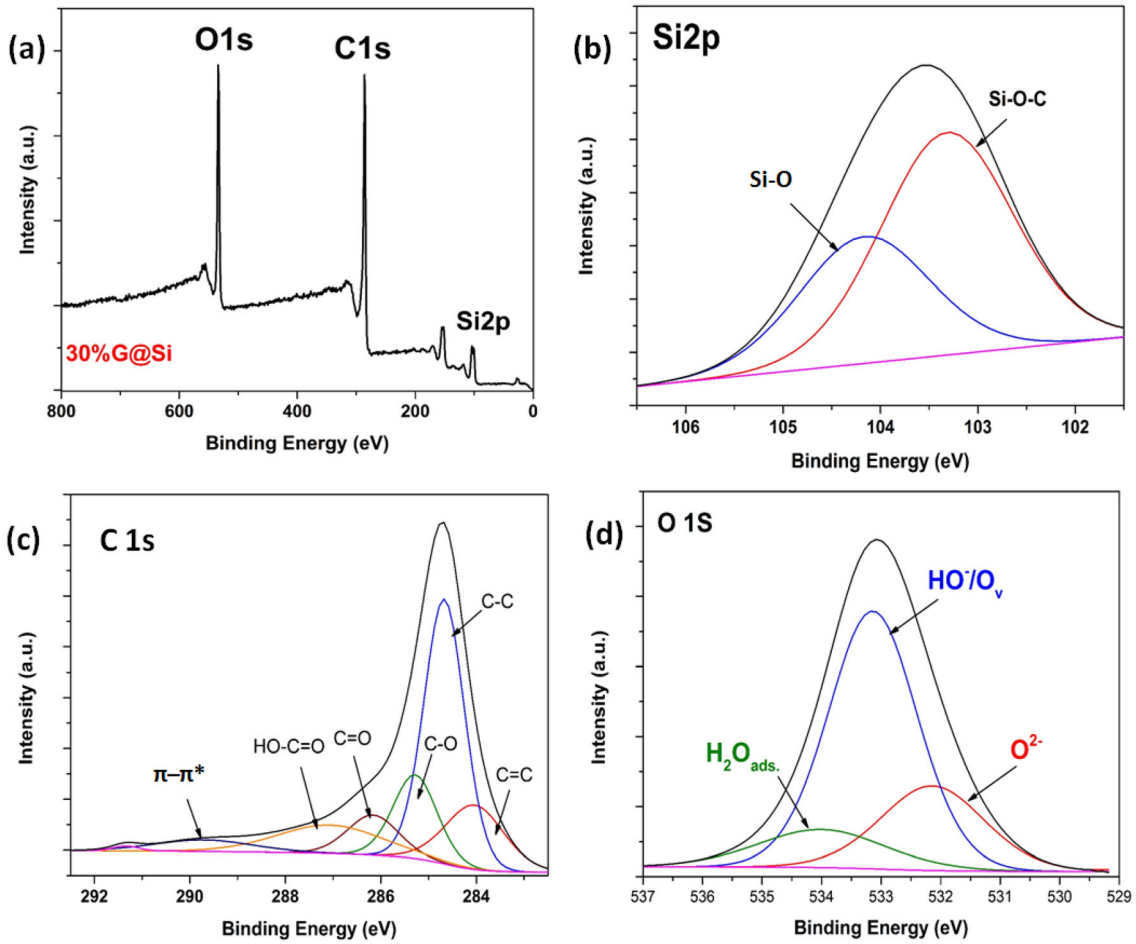

Fig. 4 **a** XPS survey of 30%G@Si composite, **b** Narrow XPS scans of Si2p, **c** C1s, and **d** O 1 s, respectively

capacity after incomplete decomposition of SEI and Li_2O or LiOH as seen in Fig. 5b and d. It is also depicted that the cathodic peaks at higher potentials in the case of 30% G@Si are overlapped in one strong peak around 0.7 V leading to lower separation distance with the corresponding anodic peak, suggesting higher reversibility and lower polarization.

Figure 6a shows the initial charge–discharge profiles for the different compositions of graphene@silicon anode materials. Electrical capacity measurements were carried out on each cell in a voltage window between 0.001 and 3 V, and the current density applied for cycling was 100 mAg^{-1} calculated with respect to the total weight of active material. The cell of pure Si anode delivered a lower discharge capacity $\sim$ 375 $mAhg^{-1}$ than those cells of all G@Si composites. As a result, the cell of 30@G/Si anode delivered the maximum discharge and charge capacities of about 1240 and 820 $mAhg^{-1}$, respectively. Plainly, each discharge curve reveals two flat potential regions at higher and lower voltages. The short plateau at high potentials > 0.5 V appears due to the decomposition of electrolyte on the surface to form the SEI layer, which is confirmed by a small plateau region at $\sim$ 0.5 V [46]. Meanwhile, the second long flat plateau at low potentials < 0.5 V corresponds to the insertion of Li^+ ions and formation of Li_xSi as explained by Eq. 1 [47]. Figure 6b shows the profiles of the discharge capacity vs. the cycle number of all cells cycled at 100 mAg^{-1} up to 100 cycles. Generally, all the anode materials made from G@Si composite show better electrochemical performance than pure Si anode. However, the cell with 30%G@Si demonstrates the highest discharge capacity retention 73%, delivering about 900 $mAhg^{-1}$ after 100 cycles. Alongside, pure Si and 10%G@Si anode show the highest capacity fading in comparison with other G@Si composites. In case of shielding Si particles with graphene, high reversibility is obtained because graphene nanoplates act as buffer material to

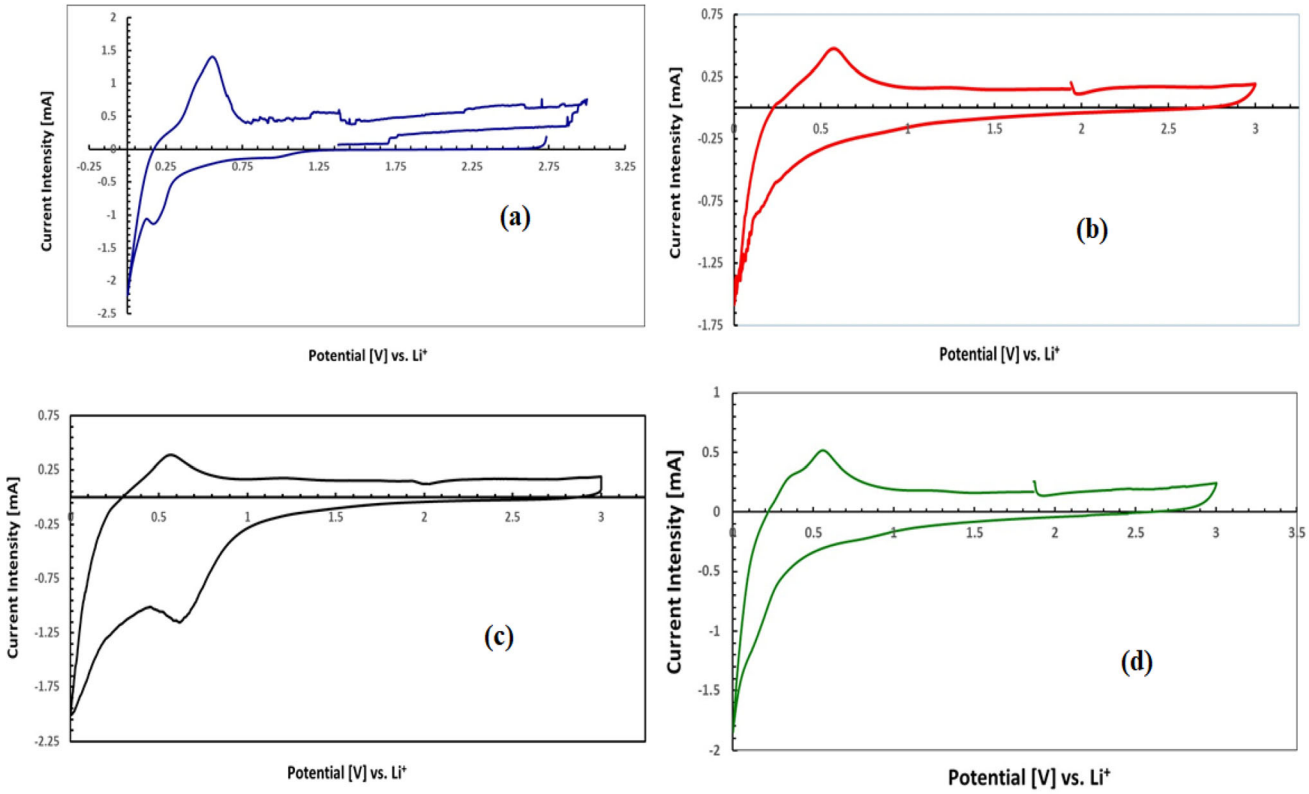

Fig. 5 CV profiles of various G@Si composites **a** 10%, **b** 20%, **c** 30%, and **d** 40% at scan rate 0.1 mV^{-1} from 0.0 to 3.0 V

minimize the large volume change of Si during charge/ discharge process [48]. Moreover, the presence of graphene in a certain amount with Si gives good mechanical flexibility and high surface area for improved accommodation of Li in Si crystal lattice. Furthermore, The tiny Si particle size coated with graphene aids in lowering the significant volume change experienced during cycling processes. One of the key methods for identifying variations in the behavior of the electrode at the electrode/electrolyte interface caused by conductivity changes is electrochemical impedance spectroscopy (EIS). Figure 6c displays the EIS spectra for the discharged cells, which comprise (i) the resistance of the electrolyte, R_e on the real Z' axis at the high frequency, (ii) the charge transfer resistance (R_{ct}) in the region of high-middle frequency, and (iii) the straight line appeared in the region of low-frequency. Interestingly, a remarkable decrease in the R_{ct} value can be observed after the addition of graphene nanoplatelets. The lithium ions diffuse into the bulk of anode material in the low-frequency region, which is known as Warburg diffusion resistance [49].

It is revealed that pure Si electrode has the maximum R_{ct} value $\sim$ 1825 Ω in comparison with various G@Si composite electrodes. This means that high graphene loadings provide a conductive pathway to decrease the charge transfer resistance of Si decreases until certain concentration of 30%G, achieving R_{ct} $\sim$ 14.8 Ω. It is also observed that increasing the graphene concentration up to 40% increases the R_{ct} to 279 Ω. i.e., the optimum ratio of graphene in preparation of these samples is 30% G with 70% Si.

Figure 6d shows the relationship between the real part of the impedance Z_{re} and the reciprocal root square of the lower angular frequency $\omega^{-0.5}$. Equation 3 explains this relationship as follows:

$$Z_{re} = R_e + R_{ct} + \sigma_w \cdot w^{-0.5}, \quad (3)$$

where: $\sigma_\omega$is the Warburg impedance coefficient

This relation depicts the resistance in the lower frequency region of the cells according to the diffusion of the Li-ions in the cells. EIS parameters are recorded in Table 1.

Values of Li^+ ions diffusion coefficient into the bulk anode materials are determined from Eq. 4.

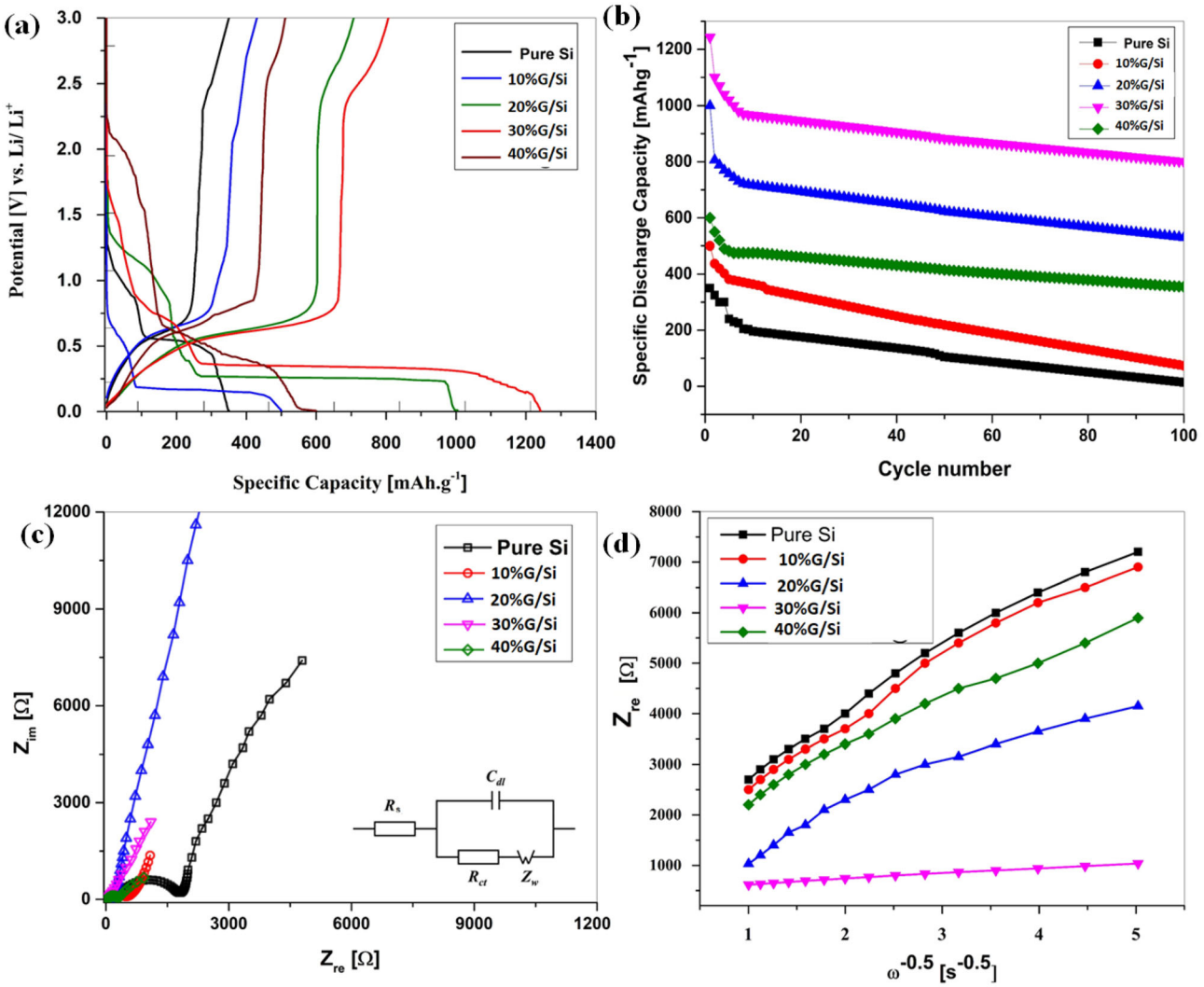

Fig. 6 **a** Capacity—voltage profiles of the first cycle at 100 mA.g^{-1} b, **b** Cycle life assessment curves up to 100 cycles, **c** EIS spectra of all samples after 1st cycle between 100 mHz and 1 0 kHz, **d** Relationships between real impedance and the reciprocal root square of the lower angular frequency for the cells of pure Si and G@Si composites (*G* = 10, 20, 30, 40wt%)

$$D = 0.5(RT/AF^2\sigma_w \cdot C)^2 \quad (4)$$

The double-layer capacitance (C_{dl}) is given by Eqns. 5 & 6:

$$Z_{re} = R_e + R_{ct} + 2\sigma_w^2 \cdot C_{dl} \quad (5)$$

$$\omega = 1/R_{ct}.C_{dl}, \quad (6)$$

where: R_{ct}: resistance of charge transfer, R_e: resistance of the electrolyte, ω: angular frequency in the low range of frequency, D: coefficient of Li-ions diffusion,

Table 1 EIS parameters of Li/Si-graphene cells with different ratios

Ratio	R_s [Ω]	R_{ct} [Ω]	σ_ω [Ω..s$^{0.5}$]	i° [A]	D [cm^{2}s^{-1}]	C_{dl} [F]
Pure Si	13.98	1.85E + 03	1119.718	1.39E-05	1.06E-13	6.84E-06
10%G@Si	7.99007	5.17E + 02	1094.835	4.97E-05	1.07E-13	1.36E-06
20%G@Si	13.3696	1.47E + 02	776.337	1.75E-04	1.27E-13	1.70E-06
30%G@Si	6.57815	14.8	104.145	1.74E-03	3.47E-13	4.87E-05
40%G@Si	24.5468	2.79E + 02	920.656	9.20E-05	1.17E-13	2.26E-07

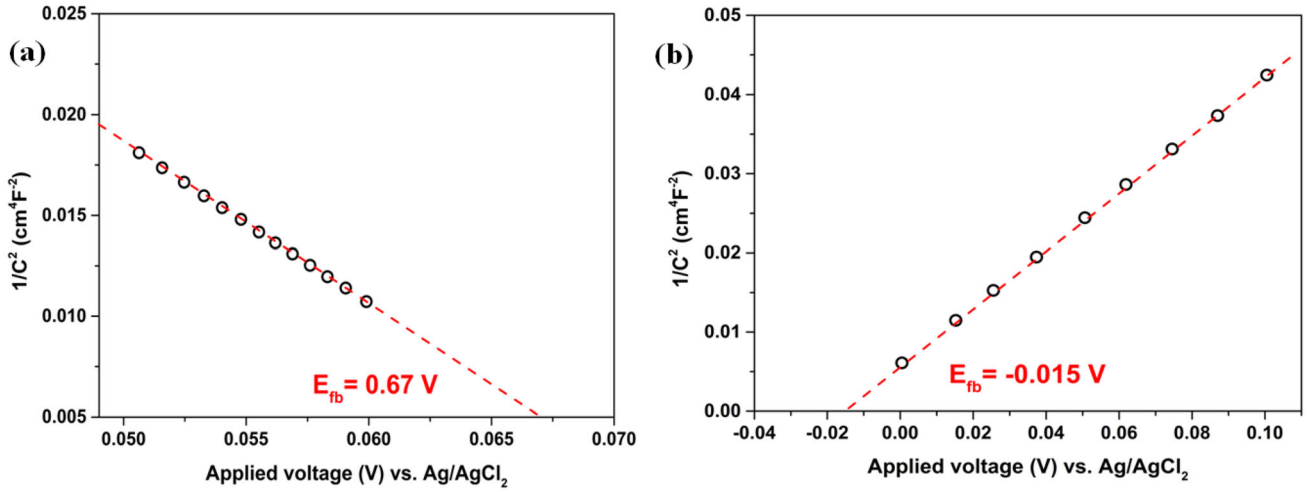

Fig. 7 Mott–Schottky plots of pure Si **a** and 30% G@Si composite **b** measured at 500 Hz

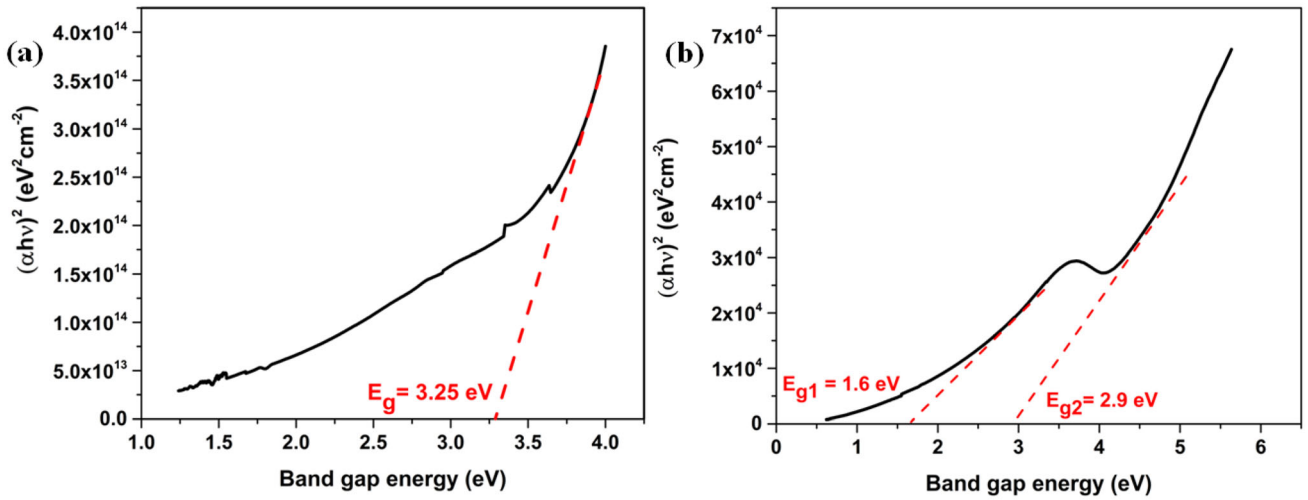

Fig. 8 Direct band gap energy plots of pure Si (**a**) and 30% G@Si composite (**b**)

R: gas constant, T: Kelvin absolute temperature, F: Faraday's constant, A: actual area of electrode, and C: concentration of Li^+ ions moles [50]. The obtained diffusion coefficient (3.47×10^{-13} cm^2s^{-1}) for the Li/30% G@Si cell explains the higher mobility of Li^+ ion diffusion than that of the other cells.

Additionally, the current density for the exchange of electrons is given by Eq. (7):

$$i^{\circ} = RT/nF, \tag{7}$$

where n: the involved electrons in the electrochemical reaction.

Accordingly, the cell with 30%G@Si has the lowest Warburg impedance coefficient ($\sigma_{\omega} \sim 104.14\ \Omega.s^{0.5}$) and the highest double-layer capacitance (C_{dl} ~ 4.87E-05 F). In general, the optimum impedance parameters are obtained with this percentage of graphene. Therefore, the charge transfer reaction of Li/ 30% G@Si electrode demonstrates the best electrochemical performance than that of the other electrodes having different ratios of G and Si.

The Mott-Schottky (M–S) characterization for the prepared samples can give us an indication about the value of the bottom level value of the conduction band, namely flat band potential (E_{fb}) [51]. Obviously, the flat band potential (E_{fb}) can be determined from the intercept of the extrapolated line with the x-axis at $1/C^2 = 0$, as displayed in M–S plot (Fig. 7). It is found that the corresponding (E_{fb}) of pure Si is about 0.67 V, suugesting a strong p-type conduction behavior. Meanwhile, the 30% G@Si possesses more negative value ~ − 0.015 V, which suggest the

conversion of electrical conduction of pure Si material into P–N type semiconductor. The obtained M–S results are comparable to the previous literature [52, 53].

The direct band gap energy of each sample can be obtained from the diffuse reflectance spectra of solid samples and the corresponding Tauc's plots (Fig. 8a and b) using kubelka–munk Eq. (8): $F(R) = (1 - R)^2/2R$ [54]. It is seen that the estimated band gap energy of pure Si sample for direct transitions is about 3.25 eV which is close to the reported value [55]. Meanwhile, the composite sample 30% G@Si indicates two band gap energy values 2.9 and 1.6 eV, which are related to the presence of major silicon and minor graphene phases. This means that the addition of graphene enhanced the electronic transitions by creating lower energy levels which improved the electrical conductivity of pure silicon. The assembled coin cell 2032 prototypes in this work is suitable for applications in small electronic devices such as electronic toys, laser pointers, digital calculators, LED flashlights, …etc.

4 Conclusions

Various compositions of graphene@silicon anode materials were prepared via physical in-situ planetary milling technique. XPS spectra of O1s suggest the partial oxidation of graphene and silicon into graphene oxide and silicon dioxide. The cell of 30%@G/Si anode delivered the maximum discharge and charge capacities of about 1240 and 820 $mAhg^{-1}$, respectively. EIS measurements revealed that 30%@G/Si anode has the highest value of Li^+ ion diffusion coefficient ($D \sim 3.47 \times 10^{-13} cm^2 s^{-1}$) and the lowest value of charge transfer resistance ($R_{ct} \sim 14.8\Omega$) in comparison with other composite materials. Accordingly, a critical amount of graphene is needed to be mixed with Si to provide high mechanical flexibility in the silicon crystals and high surface area for deep accommodation of Li^+ ions in the Si lattice. Furthermore, the small particle size of Si decorated with graphene help in decreasing of the large volume change during the cycling steps.

Acknowledgements

Not applicable.

Author contributions

MMSS participated in the experimental work and electrochemical measurements, wrote and reviewed the manuscript. AYS carried out the methodology and characterization tests and wrote the first draft of manuscript.

Funding

Open access funding provided by The Science, Technology & Innovation Funding Authority (STDF) in cooperation with The Egyptian Knowledge Bank (EKB). The authors extend their appreciation to the Science and Technology Development Fund (STDF) project with ID No. 25570.

Data availability

The authors confirm that all data generated or analyzed during this study are included in this published article.

Declarations

Conflict of interest The authors declare that they have no conflict of interest or any competing interest.

Ethical approval All the carried out experiments did not involve any human tissue and did not require any ethical approval.

Consent to participate All authors declare their consent and acceptance for participation in the present work.

Consent for publication All authors declare their consent for publication the submitted manuscript.

References

1. J. Duan, X. Tang, H. Dai et al., Building safe lithium-ion batteries for electric vehicles: a review. Electrochem. Energ. Rev. **3**, 1–42 (2020)
2. M.M.S. Sanad, N.K. Meselhy, H.A. El-Boraey, A. Toghan, Controllable engineering of new ZnAl2O4-decorated LiNi0·8Mn0·1Co0·1O2 cathode materials for high performance lithium-ion batteries. J. Mater. Res. Technol. **23**, 1528–1542 (2023)
3. S. Ge, R.S. Longchamps, T. Liu, J. Liao, Y. Leng, C.-Y. Wang, High safety and cycling stability of ultrahigh energy lithium ion batteries. Cell Rep. Phys. Sci. **2**, 100584 (2021)
4. A.Y. Shenouda, M.M.S. Sanad, "Synthesis, characterization and electrochemical performance optimization of $Li_2Ni_xFe_{1-x}SiO_4$ cathode materials for lithium-ion batteries", Bulletin of Material. Science **40**, 1055–1060 (2017)
5. S.I. Ahmed, M.M.S. Sanad, Maghemite-based anode materials for Li-Ion batteries: the role of intentionally incorporated vacancies and cation distribution in electrochemical energy storage. J. Alloy. Compd. **861**, 157962 (2021)
6. M.M. Ghannam, Z.K. Heiba, M.M.S. Sanad et al., Functional properties of $ZnMn_2O_4$/MWCNT/graphene nanocomposite as anode material for Li-ion batteries. Appl. Phys. A **126**, 332 (2020)
7. M. Obrovac, L. Krause, Reversible cycling of crystalline silicon powder. J. Electrochem. Soc. **154**, A103–A108 (2007)
8. C. Chan, H. Peng, G. Liu et al., High-performance lithium battery anodes using silicon nanowires. Nature Nanotech **3**, 31–35 (2008)
9. L. Pan, H. Wang, D. Gao, S. Chen, L. Tan, L. Li, Facile synthesis of yolk–shell structured Si–C nanocomposites as anodes for lithium-ion batteries. Chem. Commun. **50**, 5878–5880 (2014)
10. S.D. Beattie, D. Larcher, M. Morcrette, B. Simon, J.-M. Tarascon, Si electrodes for Li-ion batteries—a new way to look at an old problem. J. Electrochem. Soc. **155**, A158–A163 (2008)
11. Bo. Liang, Y. Liu, Xu. Yunhua, Silicon-based materials as high capacity anodes for next generation lithium ion batteries. J. Power Sources **267**, 469–490 (2014)
12. H.K. Liu, Z. Guo, J. Wang, K. Konstantinov, Si-based anode materials for lithium rechargeable batteries. J. Mater. Chem. **20**, 10055–10057 (2010)
13. S.R. Yousefi, H.A. Alshamsi, O. Amiri, M. Salavati-Niasari, Synthesis, characterization and application of Co/Co_3O_4 nanocomposites as an effective photocatalyst for discoloration of organic dye contaminants in wastewater and antibacterial properties. J. Mol. Liq. **337**, 116405 (2021)
14. S.R. Yousefi, A. Sobhani, H.A. Alshamsi, M. Salavati-Niasari, Green sonochemical synthesis of $BaDy_2NiO_5/Dy_2O_3$ and $BaDy_2NiO_5$/NiO nanocomposites in the presence of core almond as a capping agent and their application as photocatalysts for the removal of organic dyes in water. RSC Adv. **11**, 11500–11512 (2021)
15. S.R. Yousefi, A. Sobhani, M. Salavati-Niasari, A new nanocomposite superionic system ($CdHgI_4/HgI_2$): synthesis, characterization and experimental investigation. Adv. Powder Technol. **28**, 1258–1262 (2017)
16. S.R. Yousefi, D. Ghanbari, M. Salavati-Niasari, M. Hassanpour, Photo-degradation of organic dyes: simple chemical synthesis of $Ni(OH)_2$ nanoparticles, Ni/$Ni(OH)_2$ and Ni/NiO magnetic nanocomposites. J. Mater. Sci.: Mater. Electron. **27**, 1244–1253 (2016)
17. H. Kim, M. Seo, M.-H. Park, J. Cho, A critical size of silicon nano-anodes for lithium rechargeable batteries. Angew. Chem., Int. Ed. **49**, 2146–2149 (2010)
18. N. Liu, H. Wu, M.T. McDowell, Y. Yao, C. Wang, Y. Cui, Engineering empty space between Si nanoparticles for lithium-ion battery anodes. Nano Lett. **12**, 3315–3321 (2012)
19. L.Y. Yang, H.Z. Li, J. Liu, Z.Q. Sun, S.S. Tang, M. Lei, Dual yolk-shell structure of carbon and silica-coated silicon for high-performance lithium-ion batteries. Sci. Rep. **5**, 10908 (2015)
20. J. Graetz, C. Ahn, R. Yazami, B. Fultz, Highly reversible lithium storage in nanostructured silicon. Electrochem. Solid-State Lett. **6**, A194–A197 (2003)
21. N. Liu, Z. Lu, J. Zhao, M.T. McDowell, H.-W. Lee, W. Zhao, Y. Cui, A pomegranate-inspired nanoscale design for large-volume-change lithium battery anodes. Nat. Nanotechnol. **9**, 187–192 (2014)
22. R. Yi, F. Dai, M.L. Gordin, S. Chen, D. Wang, Micro-sized Si-C composite with interconnected nanoscale building blocks as high-performance anodes for practical application in lithium-ion batteries. Adv. Energy Mater. **3**, 295–300 (2013)
23. H. Kim, E.-J. Lee, Y.-K. Sun, R. Yi, F. Dai, M.L. Gordin, S. Chen, D. Wang, Micro-sized Si-C composite with interconnected nanoscale building blocks as high-performance anodes for practical application in lithium-Ion batteries. Adv. Energy Mater. **3**, 295–300 (2013)

24. N. Liu, K. Huo, M.T. McDowell, J. Zhao, Y. Cui, Rice husks as a sustainable source of nanostructured silicon for high performance Li-ion battery anodes. Sci. Rep. **2013**, 3 (1919)
25. W.J. Choi, M. Reddyprakash, C. Loka, Y.W. Jo, K.-S. Lee, Carbon coated Si-metal silicide composite anode materials prepared by high-energy milling and carburization for Li-Ion rechargeable batteries. J. Electrochem. Soc. **166**(3), A5131–A5138 (2019)
26. D.-H. Lee, H.-W. Shim, D.-W. Kim, Facile synthesis of heterogeneous Ni-Si@C nanocomposites as high-performance anodes for Li-ion batteries. Electrochim. Acta **146**, 60–67 (2014)
27. Z. Guojun, H. Naigen, Synthesis and properties of Si/Ag and Si/Ag/CMS composites as anode materials for Li-ion batteries. SILICON **11**, 2517–2520 (2019)
28. N.-S. Choi, K.H. Yew, K.Y. Lee, M. Sung, H. Kim, S.-S. Kim, Effect of fluoroethylene carbonate additive on interfacial properties of silicon thin-film electrode. J. Power Sour. **16**(1), 1254–1259 (2006)
29. A. Magasinski, B. Zdyrko, I. Kovalenko, B. Hertzberg, R. Burtovyy, C.F. Huebner, T.F. Fuller, I. Luzinov, G. Yushin, Toward efficient binders for Li-ion battery Si-based anodes: polyacrylic acid. ACS Appl. Mater. Interfaces **2**, 3004–3010 (2010)
30. I. Kovalenko, B. Zdyrko, A. Magasinski, B. Hertzberg, Z. Milicev, R. Burtovyy, I. Luzinov, G. Yushin, A major constituent of brown algae for use in high-capacity Li-ion batteries. Science **334**, 75–79 (2011)
31. S. Sim, P. Oh, S. Park, J. Cho, Critical thickness of SiO_2 coating layer on core@shellbulk@nanowire Si anode materials for Li-ion batteries. Adv. Mater. **25**, 4498–4503 (2013)
32. M.L. Terranova, S. Orlanducci, E. Tamburri, V. Guglielmottiand, M. Rossi, Si/C hybrid nanostructures for Li-ion anodes: an overview. J. Power Sour. **246**, 167–177 (2014)
33. X. Su, Q. Wu, J. Li, X. Xiao, A. Lott, W. Lu, B.W. Sheldon, J. Wu, Silicon-based nanomaterials for lithium-ion batteries: a review adv. Energy Mater. **4**, 1300882 (2014)
34. M.K. Kim, W.H. Shin, H.M. Jeong, Protective carbon-coated silicon nanoparticles with graphene buffer layers for high performance anodes in lithium-ion batteries. Appl. Surf. Sci. **467–468**, 926–931 (2019)
35. S. You, H.T. Tan, L. Wei, W. Tan, C.C. Li, Design strategies of Si/C composite anode for lithium-ion batteries. Chem. Eur. J. **27**, 12237–12256 (2021)
36. V. Švrček, C. Pham-Huu, J. Amadou, D. Begin, M.-J. Ledoux, Filling and capping multiwall carbon nanotubes with silicon nanocrystals dispersed in SiO2-based spin on glass. J. Appl. Phys. **99**, 064306 (2006). https://doi.org/10.1063/1.2181667
37. G. Wang, J. Yang, J. Park, X. Gou, B. Wang, H. Liu, J. Yao, Facile synthesis and characterization of graphene nanosheets. J. Phys. Chem. C **112**, 8192–8195 (2008)
38. S. Zeng, W. Feng, S. Peng, Z. Teng, C. Chen, H. Zhang, S. Peng, Dual-functional SiOC ceramics coating modified carbon fibers with enhanced microwave absorption performance. RSC Adv. **9**, 30685–30692 (2019)
39. D.S. Jensen, S.S. Kanyal, N. Madaan, M.A. Vail, A. Dadson, M.H. Engelhard, M.R. Linford, Silicon (100)/SiO_2 by XPS. Surf. Sci. Spectra **20**, 36–42 (2013)
40. K. Muthoosamy, R.G. Bai, I.B. Abubakar, S.M. Sudheer, H.N. Lim, H.-S. Loh, N.M. Huang, C.H. Chia, S. Manickam, Exceedingly biocompatible and thin-layered reduced graphene oxide nanosheets using an eco-friendly mushroom extract strategy. Int. J. Nanomed. **10**, 1505–1519 (2015)
41. Z. Xing, J. Zhicheng, Y. Zhao, J. Wan, Y. Zhu, Y. Qiang, Y. Qian, One-pot hydrothermal synthesis of Nitrogen-doped graphene as high-performance anode materials for lithium ion batteries. Sci. Rep. **6**, 26146 (2016)
42. M.M.S. Sanad, A.A. Azab, T.A. Taha, Introduced oxygen vacancies in cadmium ferrite anode materials via Zn2+ incorporation for high performance lithium-ion batteries. Mater. Sci. Semicond. Process. **143**, 106567 (2022)
43. P. Guan, J. Li, T. Lu, T. Guan, Z. Ma, Z. Peng, X. Zhu, L. Zhang, Facile and scalable approach to fabricate granadilla-like porous-structured silicon-based anode for lithium ion batteries. ACS Appl. Mater. Interfaces **10**(40), 34283–34290 (2018)
44. Q. Wei, G.-C. Liu, C. Zhang, X.-J. Hong, C.-L. Song, Y. Yang, M. Zhang, W. Huang, Y.-P. Cai, Novel honeycomb silicon wrapped in reduced graphene oxide/CNT system as high-stability anodes for lithium-ion batteries. Electrochim. Acta **317**, 583–593 (2019)
45. L. Shao, J. Shu, Wu. Kaiqiang, X. Lin, P. Li, M. Shui, D. Wang, N. Long, Y. Ren, Low pressure preparation of spherical Si@C@CNT@C anode material for lithium-ion batteries. J. Electroanal. Chem. **727**, 8–12 (2014)
46. F.E. Farghaly, A.Y. Shenouda, Electrochemical behavior of negative electrode from $Co(OH)_2$ and graphene for lithium batteries. J. Mater. Sci.: Mater. Electron. (2021). https://doi.org/10.1007/s10854-021-06162-4
47. M.M.S. Sanad, M.M. Rashad, K. Powers, Enhancement of the electrochemical performance of hydrothermally prepared anatase nanoparticles for optimal use as high capacity anode materials in lithium ion batteries (LIBs). Appl. Phys. A **118**, 665–674 (2015)
48. J.K. Lee, K.B. Smith, C.M. Haynerb, H.H. Kung, Silicon nanoparticles–graphene paper composites for Li ion battery anodes. Chem. Commun. **46**, 2025–2027 (2010)

49. M.S. Moustafa, Sanad, Arafat Toghan, Chemical activation of nanocrystalline $LiNbO_3$ anode for improved storage capacity in lithium-ion batteries. Surf. Interfaces **27**, 101550 (2021)
50. M.M.S. Sanad, A.A. Azab, T.A. Taha, Inducing lattice defects in calcium ferrite anode materials for improved electrochemical performance in lithium-ion batteries. Ceram. Int. **48**, 12537–12548 (2022)
51. M.M. Sanad, T.A. Taha, A. Helal et al., Rational optimization of g-C3N4/Co3O4 nanocomposite for enhanced photodegradation of Rhodamine B dye under visible light. Environ. Sci. Pollut. Res. (2023). https://doi.org/10.1007/s11356-023-26767-y
52. P. Lv, Xu. Chaosheng, B. Peng, Design of a silicon photocatalyst for high-efficiency photocatalytic water splitting. ACS Omega **5**, 6358–6365 (2020)
53. M. Pau Gorostiza, A. Kulandainathan, R. Díaz, F. Sanz, P. Allongue, J.R. Morante, Charge exchange processes during the open-circuit deposition of nickel on silicon from fluoride solutions. J. Electrochem. Soc. **147**, 1026–1030 (2000)
54. S.W. Arafat, Z.K. Heiba, M.M.S. Sanad, H. Elshimy, H.S. AlSalem, A.M. Alenad, T.A. Taha, Nanofabrication and functional characterization of Co9-xNixS8 nanoparticles for optoelectronic applications. Opt. Mater. **129**, 112561 (2022)
55. Yu. Jieyi, J. Gao, F. Xue, Yu. Xiuhong, Yu. Hongtao, X. Dong, H. Huang, A. Ding, X. Quan, G. Cao, Formation mechanism and optical characterization of polymorphic silicon nanostructures by DC arcdischarge. RSC Adv. **5**, 68714–68721 (2015)